Energy & Environmental Materials WILEY

3D Grid of Carbon Tubes with Mn$_3$O$_4$-NPs/CNTs Filled in their Inner Cavity as Ultrahigh-Rate and Stable Lithium Anode

Shiping Zhang, Fangming Han*, Qijun Pan, Dou Lin, Xiaoguang Zhu, Cheng Shao, Gaixia Zhang, Zhaoming Wang, Shuhui Sun*, and Guowen Meng* ⓘD

Transition metal oxides are regarded as promising candidates of anode for next-generation lithium-ion batteries (LIBs) due to their ultrahigh theoretical capacity and low cost, but are restricted by their low conductivity and large volume expansion during Li$^+$ intercalation. Herein, we designed and constructed a structurally integrated 3D carbon tube (3D-CT) grid film with Mn$_3$O$_4$ nanoparticles (Mn$_3$O$_4$-NPs) and carbon nanotubes (CNTs) filled in the inner cavity of CTs (denoted as Mn$_3$O$_4$-NPs/CNTs@3D-CT) as high-performance free-standing anode for LIBs. The Mn$_3$O$_4$-NPs/CNTs@3D-CT grid with Mn$_3$O$_4$-NPs filled in the inner cavity of 3D-CT not only afford sufficient space to overcome the damage caused by the volume expansion of Mn$_3$O$_4$-NPs during charge and discharge processes, but also achieves highly efficient channels for the fast transport of both electrons and Li$^+$ during cycling, thus offering outstanding electrochemical performance (865 mAh g^{-1} at 1 A g^{-1} after 300 cycles) and excellent rate capability (418 mAh g^{-1} at 4 A g^{-1}) based on the total mass of electrode. The unique 3D-CT framework structure would open up a new route to the highly stable, high-capacity, and excellent cycle and high-rate performance free-standing electrodes for high-performance Li-ion storage.

1. Introduction

Lithium-ion batteries (LIBs) based on graphite anode have changed people's lifestyle, but their low energy densities hinder their further application.[1–3] The research and development of high-capacity anode with practical application value is the key to the further development of LIBs.[4–6] Transition metal oxides (TMO, M$_x$O$_y$: M = Fe, Co, Ni, Mn, etc.), as a type of candidate of anode materials, have attracted great attention.[7–9] In particular, Mn$_3$O$_4$ has been regarded as a promising anode material because of its high theoretical capacity (937 mAh g^{-1}), environmental friendliness, nontoxicity, and natural abundance.[10,11] Nevertheless, the critical issues of poor electrical conductivity and drastic volume variation degrade its practical performance. Especially, the solid-electrolyte interphase (SEI) on its surface constantly breaks and grows during the charge and discharge process due to the volume variation, which would cause constant electrolyte consumption and high resistance of SEI thickening.[12,13]

Nanoscale materials are proposed to solve the lithiation/delithiation-induced large volume expansion/contraction, which can protect the electrode from damage and thus result in good cycling stability. For example, nanostructured Mn$_3$O$_4$ materials, such as nanoparticles,[14] nanosheets,[15] and hollow or porous nanostructures,[16,17] have been fabricated and shown great promise. Even so, the use of Mn$_3$O$_4$ as the anode is still significantly inhibited by the intrinsic poor electrical conductivity. To enhance the conductivity and release the volume expansion simultaneously, the more effective strategy is to load active Mn$_3$O$_4$ nanomaterials onto various conductive materials (carbon nanotube (CNT),[18,19] graphene,[20,21] and porous carbon sphere[22]). For instance, Mn$_3$O$_4$@C micro/nanocuboids,[23] CNTs@Mn$_3$O$_4$ hybrid nanomaterial,[18] Mn$_3$O$_4$@CNT/TiO$_2$ hybrid structure,[19] and Mn$_3$O$_4$ nanotubes@pGS composite[21] could exhibit pretty good cycling and rate performance. However, it should be noted that the reversible specific capacities of these electrodes are mostly calculated based on the mass of the active materials. Once we consider binders, conductive agents, and metal collectors, the electrode capacity will decrease significantly. In response to the issue, a pretty good solution is to construct self-supported electrodes by electrostatic spinning[24] and the vacuum filtration method.[25] For instance, a highly flexible graphene/Mn$_3$O$_4$

Dr. S. Zhang, Prof. F. Han, Dr. Q. Pan, Dr. D. Lin, X. Zhu, C. Shao,
Prof. G. Zhang, Z. Wang, Prof. S. Sun, Prof. G. Meng
Key Laboratory of Materials Physics, and Anhui Key Laboratory of
Nanomaterials and Nanotechnology, Institute of Solid State Physics, HFIPS,
Chinese Academy of Sciences, P. O. Box 1129, Hefei 230031, China
E-mail: fmhan@issp.ac.cn
E-mail: gwmeng@issp.ac.cn
Dr. S. Zhang, Prof. F. Han, Dr. Q. Pan, Dr. D. Lin, Prof. G. Meng
Department of Materials Science and Engineering, University of Science and
Technology of China, Hefei 230026, China
Prof. G. Zhang
Department of Electrical Engineering, École de Technologie Supérieure (ÉTS),
Montréal, Québec H3C 1K3, Canada
Prof. S. Sun
Institut National de la Recherche Scientifique (INRS), Centre Énergie,
Matériaux Télécommunications, Varennes, Québec J3X 1P7, Canada
E-mail: shuhui.sun@inrs.ca
ⓘD The ORCID identification number(s) for the author(s) of this article can
be found under https://doi.org/10.1002/eem2.12586.

nanocomposite membrane synthesized by a simple vacuum filtration method delivers a high specific capacity of $\sim$800 mAh g^{-1} at 0.1 A g^{-1} based on the total electrode mass.[25] However, even for conductive frameworks made of carbon nanomaterials, the contact resistance between the nanomaterials and the stability of the frameworks will also degrade the device's performance. Therefore, a 3D integrated carbon framework should be proposed as a promising framework for active materials, to enhance the conductivity and stability, buffer the volume expansion, also avoid the use of binders, conductive agents, and metal collectors, which could result in superior performance at the electrode level.[25–29]

Herein, we report a free-standing 3D chemical-bonding interconnected carbon tube (3D-CT) framework with Mn_3O_4 nanoparticles (Mn_3O_4-NPs) and CNTs composites (Mn_3O_4-NPs/CNTs) filled in the inner cavities of the CTs (denoted as Mn_3O_4-NPs/CNTs@3D-CT), which could efficiently release the expansion of Mn_3O_4 and protect SEI from damage. Used as the anode of LIBs, the Mn_3O_4-NPs/CNTs@3D-CT framework anode exhibits excellent cycling and rate performance. A high reversible capacity of 865 mAh g^{-1} is demonstrated at a current density of 1 A g^{-1} after 300 cycles. Even at a high current density of 4 A g^{-1}, a reversible capacity of 418 mAh g^{-1} is still remained, which is the pretty high value of all reported Mn_3O_4 anodes. This excellent electrochemical performance can be attributed to the following two aspects: the role of the free-standing chemical-bonding integrated 3D-CT grid and the inner much smaller diameter CNTs. The 3D-CT framework can provide high structural stability, superior electrical conductivity, and efficient ion transport channels, while the inner much smaller diameter CNTs can provide great conductive paths between Mn_3O_4-NPs and 3D-CT grid. Mn_3O_4-NPs are filled in the interior of CTs, which ensures that the SEI membrane on the free-standing 3D-CT grid surface is free from the interference of volume changes in Mn_3O_4 and maintains a stable morphology. Furthermore, due to the complicated valence states of Mn in Mn_3O_4, the phenomenon that part of the original Mn_3O_4 would be transformed to MnO and MnO_2 during the charge and discharge process is discovered, which would be helpful to understand the reaction mechanisms of Mn_3O_4-based anodes. Conclusively, this unique structure would open up a new route to the development of the high-performance anode for LIBs.

2. Results and Discussion

As depicted in **Figure 1**, the synthetic procedure of the free-standing Mn_3O_4-NPs/CNTs@3D-CT grid films follows consecutive steps. Firstly, the 3D-nanoporous anodic aluminum oxide (AAO) template was prepared by a simple anodization process and the diameters of nanochannels can be regulated by the anodization voltage.[30] Then, the carbon layer was grown on the surface of the 3D-nanoporous AAO template by chemical vapor deposition (CVD) and its thickness could be controlled by the deposition time.[30] Through a simple wet chemistry and secondary CVD method, Mn_3O_4-NPs and CNTs were filled in the cavities of the 3D-CT, and followed by removing the AAO template. The mass loading of Mn_3O_4 can be adjusted by the concentration of Mn $(NO_3)_2$ aqueous solution. Finally, the Mn_3O_4-NPs/CNTs@3D-CT grid film with a diameter of 14 mm was obtained, as shown in Figure 1b. Good chemical-bonding connections between the vertical CTs and the lateral CTs can ensure good structural stability and facilitate electron transport efficiently.[30] Moreover, the vertical CTs can shorten the

transport distance of Li$^+$ (Figure 1c), while the presence of CNTs and enough void space inside the CTs can alleviate the expansion of Mn_3O_4-NPs and protect SEI membrane on the surface of CTs from damage (Figure 1d).

The morphologies of the 3D-nanoporous AAO template, 3D-CT, MnO_2-NPs@3D-CT, and Mn_3O_4-NPs/CNTs@3D-CT grids are characterized by SEM (**Figure 2**, Figures S1 and S2, Supporting Information). The thickness of the 3D-nanoporous AAO template is about 20 µm (Figure S1a, Supporting Information). Besides the traditional highly ordered vertical cylindrical pores in the AAO template, there are plenty of lateral pores on the pore walls of the vertical cylindrical nanochannels, which interconnect adjacent vertical cylindrical nanochannels. The lateral pores can be ascribed to the accumulation and then removal of the Cu-containing nanoparticles during the anodization process[31,32] (Figure S1b, Supporting Information). After CVD growth of CT and then selectively etching the AAO template, the free-standing 3D-CT grid film is obtained, as shown in Figure 2a. The vertical CTs are connected with each other by many lateral CTs to form a free-standing stable scaffold structure, and the diameters of the vertical CTs and the lateral CTs are about $\sim$200 and 100 nm, respectively (Figure 2b). After the deposition of MnO_2, numerous nanoparticles are anchored on the inner walls of the 3D-CT (Figure S2, Supporting Information). However, these nanoparticles are distributed unevenly and agglomerated, which would be harmful to the stability and the conductivity of the active material, and then to the conductivity and the electrochemical properties of MnO_2-NPs@3D-CT. Luckily, after secondary CVD of CNTs, the morphology of Mn_3O_4-NPs/CNTs@3D-CT is analogous to that of 3D-CT and still remains a stable scaffold structure. Simultaneously, it can be clearly observed that the CNTs spread out from the cavities of 3D-CT (Figure S3, Supporting Information). The Mn_3O_4 nanoparticles are redistributed and decorated more separately on the inner walls of the vertical and lateral CTs due to the generation of CNTs, while there is no particle found on the outer surface of CTs (Figure 2c).

The Raman spectra of 3D-CT, MnO_2-NPs@3D-CT, and Mn_3O_4-NPs/CNTs@3D-CT are displayed in Figure 2d. Different from 3D-CT grids, the other two grids show three characteristic peaks centered at 646, 1348, and 1591 cm^{-1}. The former peak can be assigned to MnO lattice vibrations, while the latter two belong to the D and G bands of graphitic carbon.[33] X-ray diffraction (XRD) patterns in Figure 2e show that besides the broad peak of amorphous carbon from 3D-CT, the MnO_2-NPs@3D-CT, and Mn_3O_4-NPs/CNTs@3D-CT grids also have some obvious diffraction peaks, corresponding to the standard peaks of MnO_2 (PDF#01-072-1982) and Mn_3O_4 (PDF#01-089-4837), respectively. Therefore, it is also demonstrated that the MnO_2-NPs have transformed into Mn_3O_4-NPs during the secondary CVD process. Furthermore, X-ray photoelectron spectroscopy (XPS) is performed to qualitatively analyze the chemical composition and valence states of the Mn_3O_4-NPs/CNTs@3D-CT grid. The survey spectrum (Figure S4a, Supporting Information) confirms the existence of Mn, C, and O elements. Two strong peaks centered at 642.3 and 653.9 eV are attributed to Mn$2p_{3/2}$ and Mn$2p_{1/2}$, respectively (Figure S4b, Supporting Information). According to the peak's position and intensity ratio of Mn$2p_{3/2}$ and Mn$2p_{1/2}$, the manganese might exist as Mn^{2+} and Mn^{3+} states in the Mn_3O_4-NPs.[34]
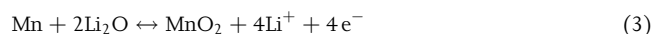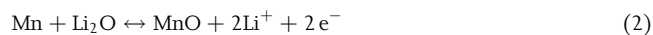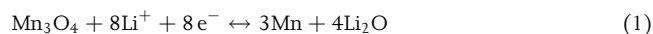
The TEM image in Figure 2f shows that numerous Mn_3O_4-NPs and CNTs are intertwined and filled inside the cavities of the CTs. The CNTs are derived from the secondary CVD process with a little bit of Mn-based nanoparticles as catalysts, produced by carbothermal reduction of MnO_2.[35] It is worth mentioning that these CNTs can not only
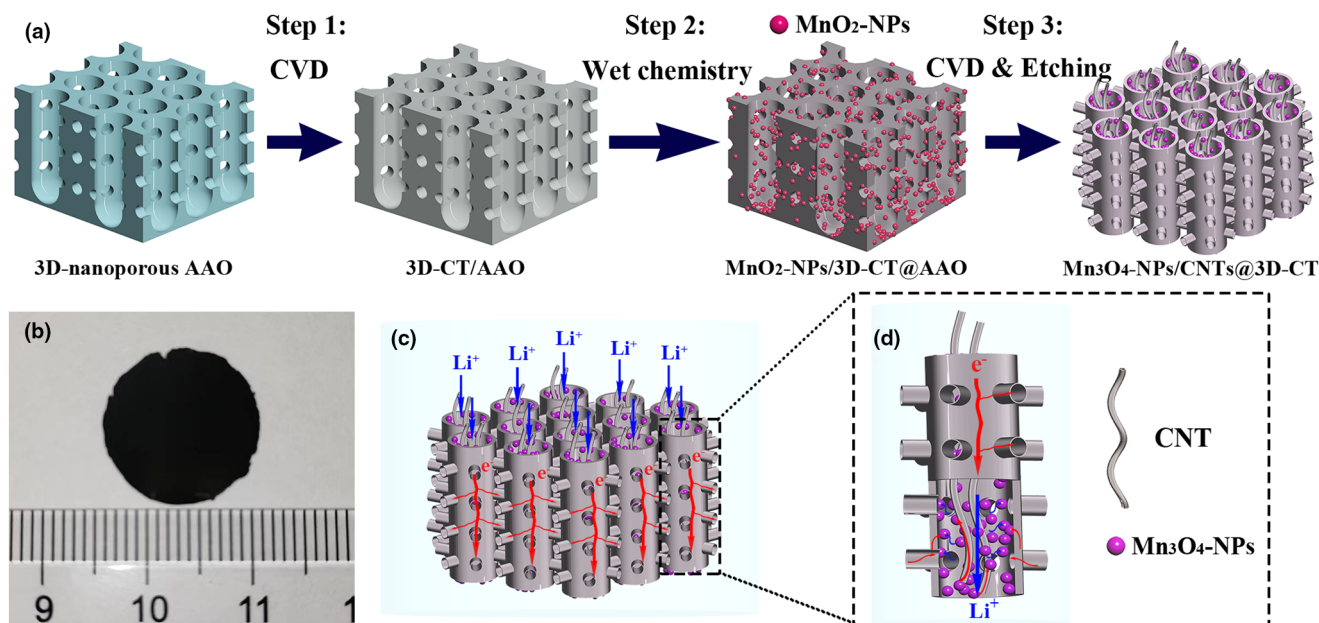
Figure 1. Schematic of the Mn_3O_4-NPs/CNTs@3D-CT grid film anode. a) the synthetic procedure. b) Optical image. c) Li^+ and electrons transport route. d) Li^+ and electrons transport in a single vertical CT.

effectively alleviate the expansion of Mn_3O_4 but also improve the electrical contact between Mn_3O_4-NPs and the 3D-CT framework. The HRTEM image shows 0.246 nm lattice spacing of the (202) planes of Mn_3O_4, and the diameter of the particle is about 10 nm. The EDS images (Figure 2g) of the CTs also provide clear evidence of the coexistence and distribution of Mn, O, and C elements. Furthermore, the Mn_3O_4-NPs/CNTs@3D-CT films with different Mn_3O_4 mass loadings (denoted as Mn_3O_4-X-NPs/CNTs@3D-CT according to the concentration of $Mn(NO_3)_2$ solution, X means X moles) are analyzed by thermogravimetric analysis (TGA) (Figure S5, Supporting Information). It is revealed that the Mn_3O_4 contents of Mn_3O_4-1-NPs/CNTs@3D-CT, Mn_3O_4-2-NPs/CNTs@3D-CT, Mn_3O_4-3-NPs/CNTs@3D-CT samples are about 26.1%, 42.2%, and 70.5%, respectively. With the increase in $Mn(NO_3)_2$ concentration, the amount of Mn_3O_4-NPs increases, and the carbon content in the composites decreases.

The electrochemical performance of Mn_3O_4-NPs/CNTs@3D-CT anodes is first evaluated by cyclic voltammetry (CV) at a scanning rate of 0.2 mV s^{-1} (**Figure 3**a). In the first cathodic half-cycle, two broad peaks at 1.15 and 0.8 V, and a strong peak at 0.16 V are observed. These two broad peaks correspond to the formation of SEI, some side reactions between Li^+ and active materials, and the accompanying reduction of MnO_x,[25,36,37] which disappear in the second cycle, confirming that the formation of SEI occurred in the first cycle, while the strong peak at 0.16 V might be associated with the reduction of Mn_3O_4 to metallic manganese (**Equation 1**), and then it shifts to 0.3 V in the following cycles. The increased lithiation potential has been widely reported in the literature, which is ascribed to the reduced polarization of the electrode during the initial activation process.[38,39] For the initial anodic scan, a broad anodic peak is revealed at 1.3 V, which could be ascribed to the reversible electrochemical oxidation of Mn^0 to Mn_3O_4 (Equation 1). However, the subsequent data prove that it may be also related to the oxidation of Mn^0 to MnO and MnO_2 (**Equations 2** and **3**).

$$Mn_3O_4 + 8Li^+ + 8e^- \leftrightarrow 3Mn + 4Li_2O \qquad (1)$$

$$Mn + Li_2O \leftrightarrow MnO + 2Li^+ + 2e^- \qquad (2)$$

$$Mn + 2Li_2O \leftrightarrow MnO_2 + 4Li^+ + 4e^- \qquad (3)$$

The discharge–charge voltage profiles shown in Figure 3b indicate that the initial discharge and charge capacity of Mn_3O_4-NPs/CNTs@3D-CT is 1150 mAh g^{-1} and 618 mAh g^{-1}, respectively, yielding an initial Coulombic efficiency (CE) of only 53%. The irreversible capacity may be attributed to the extremely high specific surface area of 3D-CT[30] and CNTs. Although the high specific surface area is beneficial to the transport of Li^+ and the release of the electrode material's volume expansion, more SEI films would be generated in the first cycle. This irreversible reaction would consume a large amount of Li^+, resulting in a significant decrease in the initial CE (Figure S6, Supporting Information). This phenomenon has also been reported in many carbon nanotube-based cathodes.[40] Expectedly, the overlapped discharge–charge curves in the following cycles confirm the high stability, reversibility, and enhanced kinetics of the electrochemical reaction due to the stable chemical-bonding integrated 3D-CT structure.

In order to compare the electrochemical performances of 3D-CT, Mn_3O_4-NPs/CNTs@3D-CT, MnO_2-NPs@3D-CT, and CNTs@3D-CT anodes, CNTs@3D-CT anode is prepared by removing the Mn_3O_4-NPs from Mn_3O_4-NPs/CNTs@3D-CT anode, and their cycling stabilities are further evaluated by galvanostatic discharge–charge measurements (Figure 3c and Figure S7a, Supporting Information). Unless otherwise noted, all the specific capacities reported in this article are based on the total mass of the electrode. For the 3D-CT grid anode, the specific capacity is only 431.5 mAh g^{-1} after 300 cycles at the current density of 1.0 A g^{-1}. Due to the addition of CNTs, the CNTs@3D-CT grid anode can store extra Li ions in the cavities of the CNTs,[41] so it exhibits a specific capacity of 683.5 mAh g^{-1} at 1.0 A g^{-1} after 300 cycles
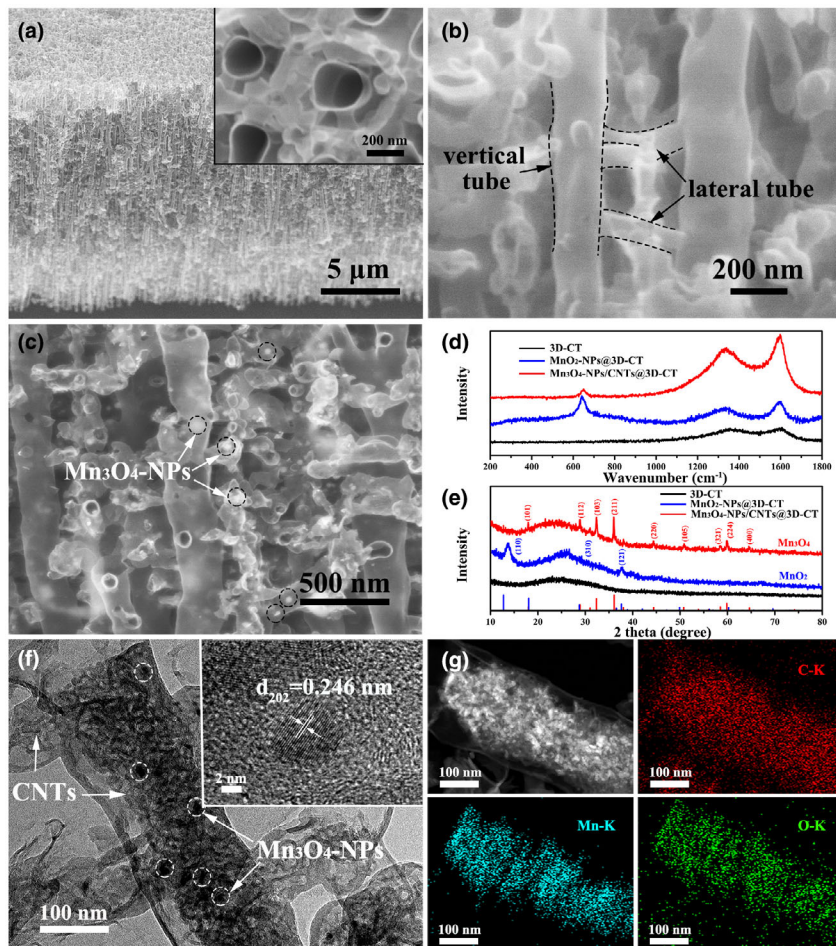
Figure 2. Structural characterization. a, b) SEM cross-sectional view and top view (Inset in a)) of 3D-CT grid. c) SEM cross-sectional view of Mn_3O_4-NPs/CNTs@3D-CT. d) Raman spectra and e) XRD patterns of 3D-CT, MnO_2-NPs@3D-CT, and Mn_3O_4-NPs/CNTs@3D-CT. f) TEM and HRTEM (Inset) images of Mn_3O_4-NPs/CNTs@3D-CT. g) TEM-EDS elemental mapping images of the Mn_3O_4-NPs/CNTs@3D-CT.

depicted in Figure 3d, the Mn_3O_4-NPs/CNTs@3D-CT anode delivers reversible capacities of 1188, 667, 619, 552, 497, and 418 mAh g^{-1} at current densities of 0.1, 0.2, 0.5, 1.0, 2.0, and 4.0 A g^{-1}, respectively. Even when the current density returns to 1 A g^{-1}, the capacity of the electrode fully recovers to 606 mAh g^{-1}. By comparison, 3D-CT, CNTs@3D-CT, and MnO_2-NPs@3D-CT anodes deliver reversible capacities of 244, 235, and 378 mAh g^{-1} at a high current density of 4.0 A g^{-1}, respectively. Compared with the other anodes, the Mn_3O_4-NPs/CNTs@3D-CT anode exhibit more superior rate performance and better reversible capacity, which could be ascribed to its unique structure. The vertical CTs of 3D-CT could promote the fast transport of electrons and ions, and CNTs in the cavity of CTs could further improve the conductivity and the stability of the active material. The high and stable specific capacity of Mn_3O_4-NPs/CNTs@3D-CT is very attractive for LIBs and much superior to those of some other Mn_3O_4-based anodes, especially at high rates (Figure S9 and Table S1, Supporting Information).

To demonstrate the reaction mechanism of Mn_3O_4-NPs/CNTs@3D-CT during the lithiation and delithiation process, in situ XRD analysis is conducted (**Figure 4a**). The XRD peaks at 32° and 35.7° correspond to the (103) and (211) planes of Mn_3O_4 fade away during the discharge process. During the consecutive discharging process, peaks assignable to Li_2O or Mn could not be detected, suggesting that the compound occurred in the form of amorphous phases.[43] However, distinctive XRD peaks for Mn_3O_4 are still weak and have no change in the following charge process, likely due to the poor crystallinity and small size of the intermediates.[44]

In order to further study the Li-ion storage mechanism of Mn_3O_4-NPs/CNTs@3D-CT anode in the process of lithiation/delithiation, ex situ XRD and XPS measurements are carried out to investigate the crystal structure and the valance state of active materials. As shown in Figure 4b, the XRD pattern of the fully delithiated sample after three cycles shows that the XRD peaks not only correspond to some planes of original Mn_3O_4, but also the (101) plane of MnO_2 and (200) plane of MnO, indicating that not all of the Mn_3O_4-NPs can be able to recover back to Mn_3O_4 during the charging process, some of them may be less oxidized to MnO (Equation 2), and others may be further oxidized to MnO_2 (Equation 3). Meanwhile, the XRD pattern of the fully lithiated sample shows that the characteristic peaks of MnO, Mn_3O_4, and MnO_2 get weak and even disappear, which might result from the reduction of MnO_x to zero-valent Mn (Mn^0), which might be dispersed in the Li_2O matrix.[45] The XPS spectrum in Figure 4c displays that the valence energy of the fully delithiated sample after three cycles is increased compared to the uncycled sample, indicating that higher valence manganese ions (Mn^{4+}) are generated as the cycles go on, which is also corresponding to the results of XRD test. The HRTEM images
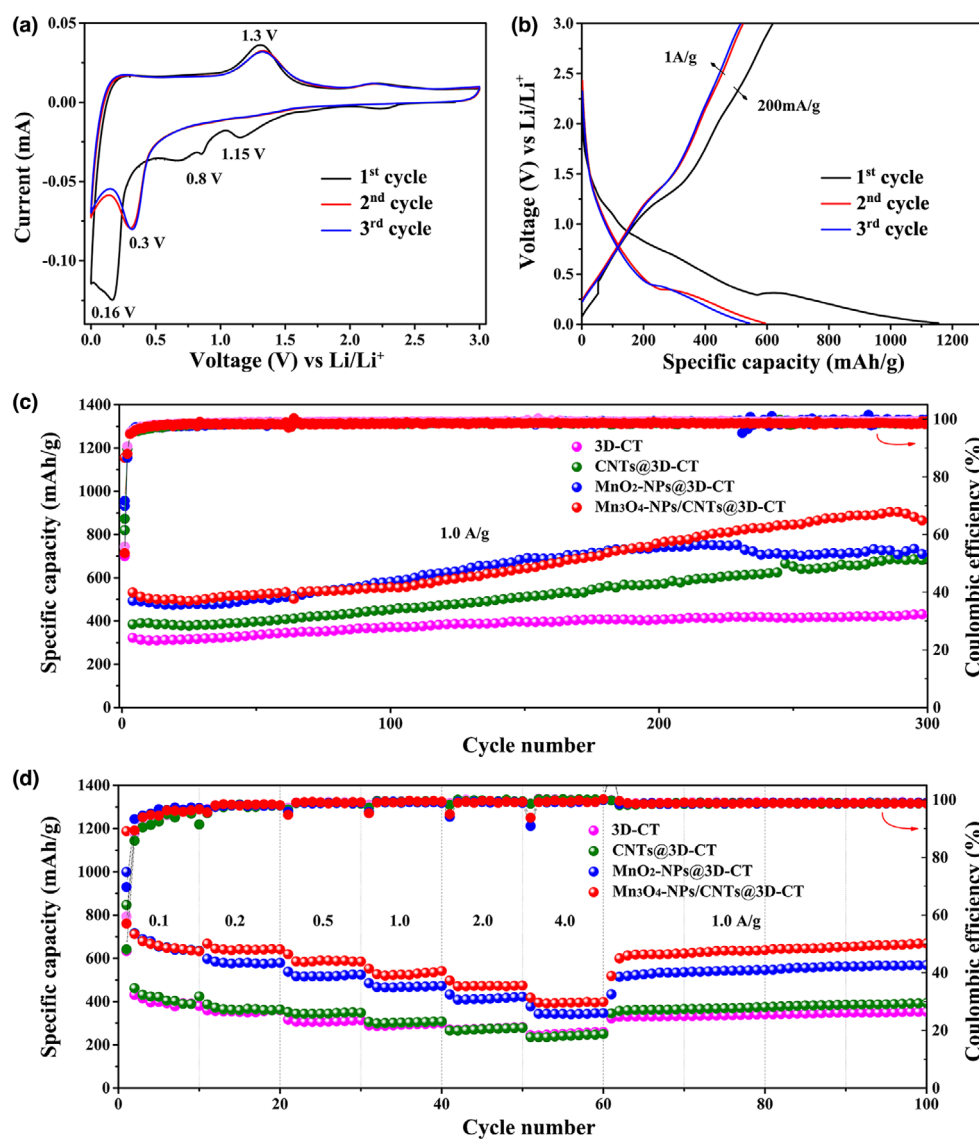
without any decay. While for the MnO_2-NPs@3D-CT anode, the specific capacity has been greatly improved due to the addition of active material and could reach 743 mAh g^{-1} after 200 cycles. Nonetheless, the specific capacity gradually decreases to 717 mAh g^{-1} in the following 100 cycles. Combing the merits of the above two anodes, the Mn_3O_4-NPs/CNTs@3D-CT grid anode delivers a specific capacity of 865 mAh g^{-1} after 300 cycles at 1.0 A g^{-1}, which is higher than that of the MnO_2-NPs@3D-CT and CNTs@3D-CT, indicating more excellent cycling stability. In order to further improve the stability of the electrode, a new lithium hexafluoropropane-1,3-disulfonimide (LiHFDF)-based electrolyte is synthesized by modifying the anion salt of traditional electrolyte.[42] As a result, Mn_3O_4-NPs/CNTs@3D-CT can be stably cycled over 1200 times even at a high current density of 2 A g^{-1}, which can be ascribed not only to the highly efficient passivation ability of the cyclic anions[42] but also to the perfect structural stability of the 3D-CT frameworks (Figure S8, Supporting Information).

The rate capabilities of 3D-CT, MnO_2-NPs@3D-CT, CNTs@3D-CT, and Mn_3O_4-NPs/CNTs@3D-CT anodes are also tested at different current densities (Figure 3d and Figure S7b, Supporting Information). As

Figure 3. Electrochemical characterization. a) Cyclic voltammetry and b) initial three charge–discharge curves of Mn$_3$O$_4$-NPs/CNTs@3D-CT anode. c) Cycling performances and d) rate capabilities of 3D-CT, CNTs@3D-CT, MnO$_2$-NPs@3D-CT, and Mn$_3$O$_4$-NPs/CNTs@3D-CT anodes.

mechanism for transition metal oxide electrodes (Figure S10b, d, Supporting Information). The nanosized effect can further reduce the dimensions of active materials and then shorten the Li-ion diffusion distance, which is also beneficial to enhance the electrode kinetics. Furthermore, TEM-EDS mapping confirms the existence of C, Mn, and O elements in the CT framework regardless of the state of delithiation and lithiation. It should be noted that the O element in delithiated state mainly exists in the form of various oxides of manganese, and in lithiated state in the form of Li$_2$O (Figure S11, Supporting Information).

The morphology of Mn$_3$O$_4$-NPs/CNTs@3D-CT grid anode after 200 cycles is also characterized by SEM (**Figure 5**a,b). It can be seen that both the CTs and the 3D integrated structure still remain intact after 200 charge–discharge cycles, indicating great structural stability of the electrode. This may benefit the transport of electrons and Li$^+$. Moreover, the obvious R$_{ct}$ decrease and slope increase observed in the Nyquist plot after first and 200th cycle (Figure 5c), further indicate an improved charge-transfer process and mass transfer of Li$^+$ in the electrode, which is consistent with the results of SEM. These results can mainly be attributed to the high structural stability, superior electrical conductivity, and efficient Li$^+$ transport channels of the 3D-CT grid.

(Figure 4d,e) also further confirm the formation of MnO$_2$, Mn$_3$O$_4$, and MnO nanocrystals in the fully delithiated Mn$_3$O$_4$-NPs/CNTs@3D-CT anode after three cycles. The above results indicate that MnO and MnO$_2$ formed in the charging process also take part in the following Li-ion storage reaction besides Mn$_3$O$_4$ in the Mn$_3$O$_4$-NPs/CNTs@3D-CT anode.

Furthermore, by comparing TEM images of the samples with the third charged and discharged states, it is found that the wall of CT gets thicker due to the intercalation of Li ions, while Li$^+$ deintercalate, the wall of CT returns to normal, indicating that the 3D-CT grid has great chemical and structural stability (Figure S10a,c, Supporting Information). As for active materials, after the lithiation process, the original large crystalline Mn$_3$O$_4$-NPs are converted into smaller Mn-NPs that are dispersed inside the Li$_2$O matrix, which is consistent with the well-accepted reaction

Due to these merits, the Mn$_3$O$_4$-NPs/CNTs@3D-CT anode exhibits a better electrochemical performance than that of other Mn$_3$O$_4$-based anodes, especially at high rates, whether the capacity is based on the mass of electrode (Figure 5d) or active materials (Figure S12, Supporting Information). In general, the unique electrode combining the integrality, highly preferred orientation and high conductivity of the 3D-CT framework with the high activity of the Mn$_3$O$_4$, might open up a new route to design high-performance anodes for LIBs.

3. Conclusion

In summary, we successfully designed and synthesized a unique free-standing Mn$_3$O$_4$-NPs/CNTs@3D-CT grid film, which could be directly utilized as an anode without the involvement of inactive components.
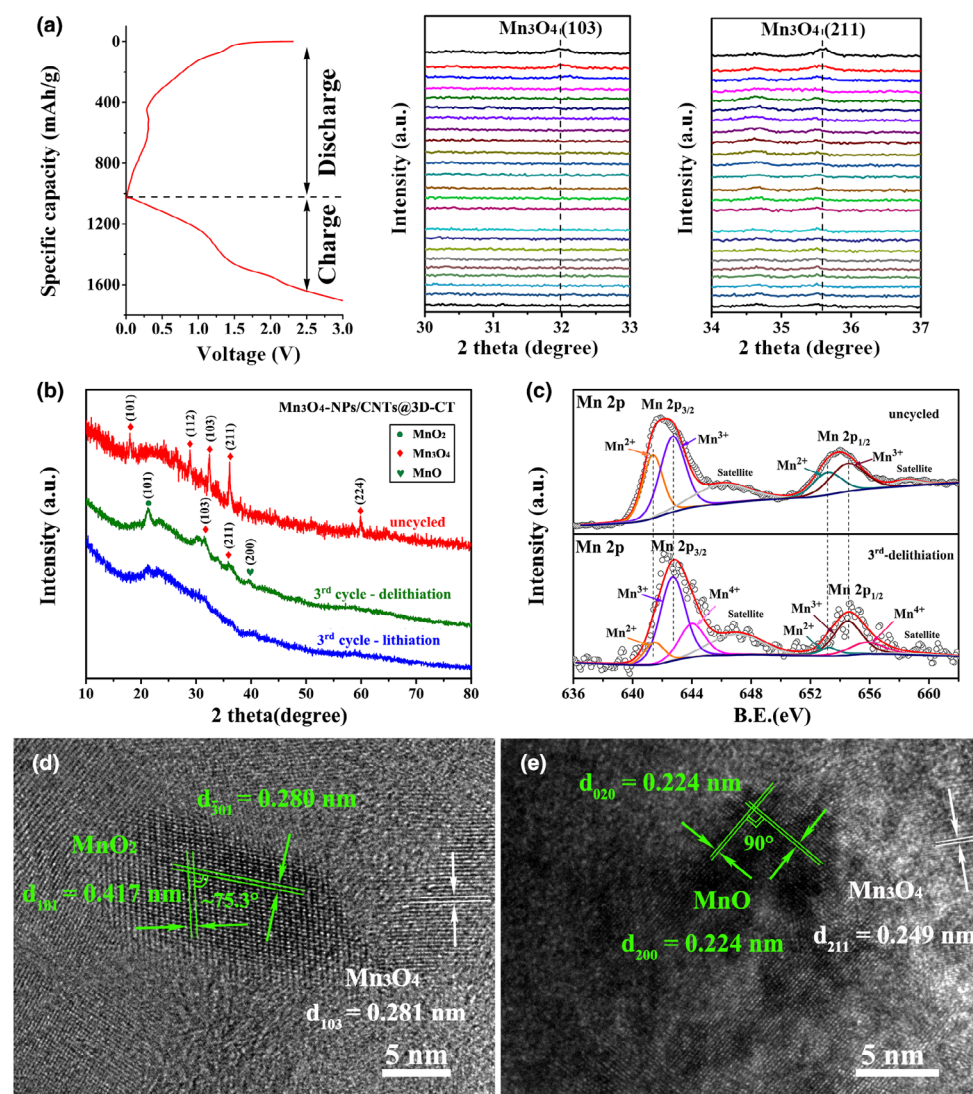
Figure 4. Li-ion storage mechanism analysis. a) In situ XRD measurements of Mn_3O_4-NPs/CNTs@3D-CT anode recorded during the first cycle at the current density of 0.1 A g^{-1} in the potential range of 0.01–3 V. b) XRD patterns of the uncycled, fully lithiated and fully delithiated Mn_3O_4-NPs/CNTs@3D-CT anode. c) Mn 2p spectra of the uncycled and fully delithiated Mn_3O_4-NPs/CNTs@3D-CT anode. d,e) HRTEM images of fully delithiated Mn_3O_4-NPs/CNTs@3D-CT anode after three cycles.

scaffold-like structure can be also further extended to other electrode materials with the integrated 3D-CT structure, and develop a new strategy of designing high-performance anodes of LIBs.

4. Experimental Section

Preparation of 3D-nanoporous AAO templates and carbon-coated 3D-nanoporous AAO templates: According to our recent work,[30] Al foil with Cu impurities (99.0% purity) was anodized under a 190 V direct current for 14 h in a mixture solution (0.3 M H_3PO_4, H_2O: C_2H_6O = 9:1 in volume) at 0 °C.[49] After removing the residual Al in a saturated $SnCl_4$ aqueous solution and selectively wet-chemical etching the Cu-containing nanoparticles embedded in the vertical nanochannel walls of the AAO template in H_3PO_4 solution, the 3D-nanoporous AAO template (denoted as 3D-nanoporous AAO, left in Figure 1a), with vertical cylindrical nanopores connected by lateral pores, was obtained.[30–32] The 3D-nanoporous AAO template was placed in a quartz boat and then inserted into a horizontal tubular furnace. After heating to 650 °C in an argon atmosphere at a rate of 10 °C min^{-1}, acetylene was introduced in the furnace at 6 sccm with an 80 sccm flow of argon carrier gas for the CVD of carbon. The acetylene was shut off after 90 min deposition, and the furnace was cooled to room temperature under the protection of an argon flow.[30] As a result, a very thin layer of carbon-coated 3D-nanoporous AAO film (denoted as 3D-CT/AAO, Figure 1a) with a diameter of 14 mm was obtained.

Preparation of MnO_2-NPs@3D-CT and Mn_3O_4-NPs/CNTs@3D-CT grid films: To achieve the different mass loadings of active materials, the above 3D-CT/AAO films were firstly immersed in 1, 2, and 3 M $Mn(NO_3)_2$ aqueous solution for 6 h at a low pressure of −0.7 Mpa compared with standard atmospheric pressure, respectively. After taken out and polished the upper surface gently using tissue, the films were dried and then heated to 300 °C at 5 °C min^{-1} in an argon atmosphere, and held at this temperature for 10 h. As a result, $Mn(NO_3)_2$ was in situ decomposed into MnO_2-NPs and loaded onto the inner cavity of the 3D-CT/AAO films (denoted as MnO_2-NPs/3D-CT@AAO, Figure 1a).[50] After that, the films were directly immersed in a 3 M NaOH solution to selectively remove the 3D-nanoporous AAO; then, MnO_2-NPs decorated on the inner cavity of 3D-CT (denoted as MnO_2-NPs@3D-CT) films were obtained. In order to further enhance the conductivity of the active materials and prevent Mn_3O_4-NPs from aggregation, a secondary CVD process was carried out onto the MnO_2-NPs/3D-CT@AAO films to in situ grow CNTs in the inner cavity of the 3D-CT for 30 min, assisted by a little bit of reduced Mn-based nanoparticles as catalyst. In the meantime, MnO_2-NPs might be transformed into Mn_3O_4-NPs (MnO_2 + C → Mn_3O_4 + CO_2)[51] under the synergistic effect of high temperature and the decomposition of acetylene. Consequently, free-standing Mn_3O_4-
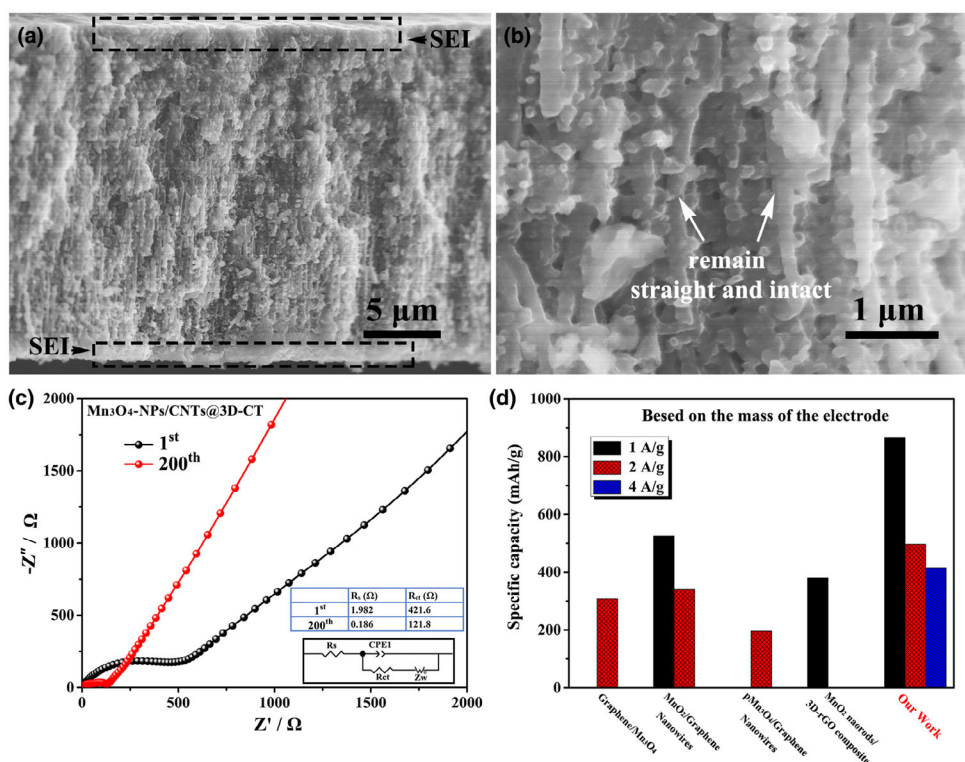
Significantly, the chemical-bonding integrated 3D-CT framework can enhance the conductivity and provide smooth ion migration. The presence of CNTs and enough void space in the inner cavity of CTs can alleviate the expansion of Mn_3O_4-NPs, keep a stable SEI membrane on the surface of the 3D-CTs grid and even establish a good conductive pathway between Mn_3O_4-NPs and the 3D-CT framework, thus leading to a high-performance anode. As a consequence, superior cycling performance (865 mAh g^{-1} at 1.0 A g^{-1} after 300 cycles) and excellent rate capability (418 mAh g^{-1} at 4 A g^{-1}) are achieved, and the capacities are calculated based on the total mass of the electrode. Moreover, part of the original Mn_3O_4 is found to be transformed into MnO and MnO_2 during the following cycle process, which may be ascribed to the complicated valence states of Mn in Mn_3O_4, and helps us to have a deeper understanding of the energy storage mechanism of Mn_3O_4-based anodes. Consequently, such unique free-standing

Figure 5. Structural evaluation and electrochemical performance of anode during cycling. a,b) SEM images of Mn$_3$O$_4$-NPs/CNTs@3D-CT anode after 200 cycles. c) Nyquist plots of Mn$_3$O$_4$-NPs/CNTs@3D-CT after the first and the 200th cycle at 1 A g^{-1}. d) Bar graph about specific capacities of Mn$_3$O$_4$-NPs/CNTs@3D-CT and previously reported Mn$_3$O$_4$ composites[25,46–48] at 1.0, 2.0, and 4.0 A g^{-1} based on the mass of electrode.

on the whole electrode mass. The cyclic voltammetry (CV) was measured on a CHI760E electrochemical workstation (Chenhua, Shanghai, China) at 0.2 mV s^{-1} between 0.01 and 3.0 V (vs Li/Li$^+$). The electrochemical impedance measurements were carried out at 5 mV AC oscillation amplitude over the frequency range of 100 kHz to 0.01 Hz.

Conflict of Interest

The authors declare no conflict of interest.

Supporting Information

Supporting Information is available from the Wiley Online Library or from the author.

NPs/CNTs@3D-CT films (right, Figure 1a) were obtained by dissolving the AAO template in a NaOH (3 M) aqueous solution.

Material characterization: The structure and morphology of the samples were characterized by scanning electron microscopy (SEM, Hitachi, SU8020), energy dispersive X-ray spectroscopy (EDS), and transmission electron microscopy (TEM, JEM-2010). The crystal structures of the as-prepared products were characterized by XRD with Cu Kα radiation (X'Pert Pro PW3040-Pro, Panalytical Inc.). Ex situ XRD analyses of Mn$_3$O$_4$-NPs/CNTs@3D-CT grid at the original state, 3rd fully discharged and charged states were performed with the above measuring equipment. The in situ XRD patterns were collected with an interval of 30 min for each 2θ scan from 10° to 45° during charge and discharge processes at 0.1 A g^{-1}, between 0.01 and 3 V versus Li/Li$^+$. Raman spectra were recorded on a confocal Raman system (Renishaw, InVia) with an excitation of 532 nm. TGA was measured on Pyris 1 Thermo gravimetric analyzer in flowing air. XPS spectra were performed by PHI 5000 Versa Probe system (Physical Electronics, MN).

Electrochemical measurement: The electrochemical performances of the samples were tested using a CR2032-type coin cell. The Mn$_3$O$_4$-NPs/CNTs@3D-CT grid films with the areal density of about 1.0 mg cm^{-2} were directly used as the working electrodes and were evaluated with respect to lithium foil (FMC Corporation) as the counter electrode. The coin cells were assembled inside an argon-filled glove box (<0.01 ppm, H$_2$O and O$_2$). The electrodes of the cells were separated by a porous polypropylene membrane (Celgard 2500) and an electrolyte solution consisting of 1.0 M LiPF$_6$ in ethylene carbonate: dimethyl carbonate: diethyl carbonate (volume ratio of 1:1:1) with 1.0% VC as a solvent mixture (DoDoChem Co. Ltd.). The electrolyte dosage for each cell is about 120–150 μL. The Galvanostatic charge–discharge test of the cells was tested on the LAND CT2001A battery system at various current densities within the voltage range of 0.01–3 V (vs Li/Li$^+$). Before cycling at high current densities, all the cells were first activated at 0.2 A g^{-1} for the first cycle. The specific capacity is calculated based

[1] X. B. Cheng, H. Liu, H. Yuan, H. J. Peng, C. Tang, J. Q. Huang, Q. Zhang, *SusMat* **2021**, *1*, 38.

[2] M. Li, J. Lu, Z. Chen, K. Amine, *Adv. Mater.* **2018**, *30*, 1800561.

[3] Y. Zhang, L. Yi, J. Zhang, X. Wang, X. Hu, W. Wei, H. Wang, *Sci. China Mater.* **2022**, *65*, 2035.

[4] F. Xin, M. S. Whittingham, *Electrochem. Energy Rev.* **2020**, *3*, 643.

[5] Z. Xu, W. Deng, X. Wang, *Electrochem. Energy Rev.* **2021**, *4*, 269.

[6] H. Yu, A. Siebert, S. Mei, R. Garcia-Diez, R. Félix, T. Quan, Y. Xu, J. Frisch, R. G. Wilks, M. Bär, C. Pei, Y. Lu, *Energy Environ. Mater.* DOI: 10.1002/eem2.12539.

[7] Y. Zhao, X. Li, B. Yan, D. Xiong, D. Li, S. Lawes, X. Sun, *Adv. Energy Mater.* **2016**, *6*, 1502175.

[8] X. Guo, G. Zhang, Q. Li, H. Xue, H. Pang, *Energy Storage Mater.* **2018**, *15*, 171.

[9] H. Xiao, S. Li, J. Zhou, C. Zhao, Y. Yuan, X. Xia, Y. Bao, M. Lourenço, K. Homewood, Y. Gao, *Energy Environ. Mater.* DOI: 10.1002/eem2.12537.

[10] L. Wang, L. Li, H. Wang, J. Yang, F. Wu, R. Chen, *ACS Appl. Energy Mater.* **2019**, *2*, 5206.

[11] X. Wang, J. Liu, Y. Hu, R. Ma, J. Wang, *Sci. China Mater.* **2022**, *65*, 1421.

[12] M. Zheng, H. Tang, L. Li, Q. Hu, L. Zhang, H. Xue, H. Pang, *Adv. Sci.* **2018**, *5*, 1700592.

[13] G. Wen, L. Tan, X. Lan, H. Zhang, R. Hu, B. Yuan, J. Liu, M. Zhu, *Sci. China Mater.* **2021**, *64*, 2683.

[14] S.-Z. Huang, J. Jin, Y. Cai, Y. Li, H.-Y. Tan, H.-E. Wang, G. Van Tendeloo, B.-L. J. N. Su, *Nanoscale* **2014**, *6*, 6819.

[15] M. Zhen, Z. Zhang, Q. Ren, L. Liu, *Mater. Lett.* **2016**, *177*, 21.

[16] W. Ma, S. Lu, X. Lei, X. Liu, Y. Ding, *J. Mater. Chem. A* **2018**, *6*, 20829.

[17] J. Zhou, T. Yang, M. Mao, W. Ren, Q. Li, *J. Mater. Chem. A* **2015**, *3*, 12328.

[18] K. Cao, Y. Jia, S. Wang, K-J. Huang, H. Liu, *J. Alloys Compd.* **2021**, *854*, 157179.

[19] W. Mao, W. Yue, Z. Xu, J. Wang, J. Zhang, D. Li, B. Zhang, S. Yang, K. Dai, G. Liu, *ACS Appl. Mater. Interfaces* **2020**, *12*, 39282.

[20] C. Liu, Q.-Q. Ren, S.-W. Zhang, B.-S. Yin, L.-F. Que, L. Zhao, X.-L. Sui, F.-D. Yu, X. Li, D.-M. Gu, Z.-B. Chem, *Eng. J.* **2019**, *370*, 1485.

[21] B. Wang, F. Li, X. Wang, G. Wang, H. Wang, J. Bai, *Chem. Eng. J.* **2019**, *364*, 57–69.

[22] L. Guo, Y. Ding, C. Qin, W. Song, S. Sun, K. Fang, W. Li, J. Du, F. Wang, *J. Alloys Compd.* **2018**, *735*, 209.

[23] Y. Jiang, J. L. Yue, Q. Guo, Q. Xia, C. Zhou, T. Feng, J. Xu, H. Xia, *Small* **2018**, *14*, 1704296.

[24] Y. Guo, D. Zhang, Z. Bai, Y. Yang, Y. Wang, J. Cheng, P. K. Chu, Y. Luo, *Dalton Trans.* **2022**, *51*, 1423.

[25] J.-G. Wang, D. Jin, R. Zhou, X. Li, X.-r. Liu, C. Shen, K. Xie, B. Li, F. Kang, B. J. A. N. Wei, *ACS Nano* **2016**, *10*, 6227.

[26] H. Wang, J. Fu, C. Wang, J. Wang, A. Yang, C. Li, Q. Sun, Y. Cui, H. Li, *Energ. Environ. Sci.* **2020**, *13*, 848.

[27] L. Hu, H. Wu, Y. Gao, A. Cao, H. Li, J. McDough, X. Xie, M. Zhou, Y. Cui, *Adv. Energy Mater.* **2011**, *1*, 523.

[28] J. Qin, Q. Zhang, Z. Cao, X. Li, C. Hu, B. Wei, *Nano Energy* **2013**, *2*, 733.

[29] C. Zhou, K. Zhang, M. Hong, Y. Yang, N. Hu, Y. Su, L. Zhang, Y. Zhang, *Chem. Eng. J.* **2020**, *385*, 123720.

[30] F. Han, O. Qian, G. Meng, D. Lin, G. Chen, S. Zhang, Q. Pan, X. Zhang, X. Zhu, B. Wei, *Science* **2022**, *377*, 1004.

[31] I. S. Molchan, T. V. Molchan, N. V. Gaponenko, P. Skeldon, G. E. Thompson, *Electrochem. Commun.* **2010**, *12*, 693.

[32] J. Vanpaemel, A. M. Abd-Elnaiem, S. De Gendt, P. M. Vereecken, *J. Phys. Chem. C* **2015**, *119*, 2105.

[33] D. Zhang, G. Li, J. Fan, B. Li, L. Li, *Chem. A Eur. J.* **2018**, *24*, 9632.

[34] A. Moses Ezhil Raj, S. G. Victoria, V. B. Jothy, C. Ravidhas, J. Wollschläger, M. Suendorf, M. Neumann, M. Jayachandran, C. Sanjeeviraja, *Appl. Surf. Sci.* **2010**, *256*, 2920.

[35] Z. Miao, J. Meng, M. Liang, Z. Li, Y. Zhao, F. Wang, L. Xu, J. Mu, S. Zhuo, J. Zhou, *Carbon* **2021**, *172*, 324.

[36] H. Wang, L.-F. Cui, Y. Yang, H. Sanchez Casalongue, J. T. Robinson, Y. Liang, Y. Cui, H. Dai, *J. Am. Chem. Soc.* **2010**, *132*, 13978.

[37] S. P. Varghese, B. Babu, R. Prasannachandran, R. Antony, M. Shaijumon, *J. Alloys Compd.* **2019**, *780*, 588.

[38] J. Guo, Q. Liu, C. Wang, M. R. Zachariah, *Adv. Funct. Mater.* **2012**, *22*, 803.

[39] F. Ma, A. Yuan, J. Xu, *ACS Appl. Mater. Interfaces* **2014**, *6*, 18129.

[40] S. Ko, J.-I. Lee, H. S. Yang, S. Park, U. Jeong, *Adv. Mater.* **2012**, *24*, 4451.

[41] G. Yang, Z. Liu, S. Weng, Q. Zhang, X. Wang, Z. Wang, L. Gu, L. Chen, *Energy Storage Mater.* **2021**, *36*, 459.

[42] Y. Hu, L. Fan, A. M. Rao, W. Yu, C. Zhuoma, Y. Feng, Z. Qin, J. Zhou, B. Lu, *Natl. Sci. Rev.* **2022**, *9*, nwac134.

[43] G. D. Park, S. J. Yang, J. H. Lee, Y. C. Kang, *Small* **2019**, *15*, 1905289.

[44] A. Varzi, L. Mattarozzi, S. Cattarin, P. Guerriero, S. Passerini, *Adv. Energy Mater.* **2018**, *8*, 1701706.

[45] Q. Li, H. Li, Q. Xia, Z. Hu, Y. Zhu, S. Yan, C. Ge, Q. Zhang, X. Wang, X. Shang, S. Fan, Y. Long, L. Gu, G.-X. Miao, G. Yu, J. S. Moodera, *Nat. Mater.* **2021**, *20*, 76.

[46] H. S. Kim, D. W. Kim, S.-S. Kim, C. Senthil, H. Y. Jung, *Chem. Eng. J.* **2022**, *427*, 130937.

[47] S.-K. Park, C.-Y. Seong, S. Yoo, Y. Piao, *Energy* **2016**, *99*, 266.

[48] H. Liu, Z. Hu, Y. Su, H. Ruan, R. Hu, L. Zhang, *Appl. Surf. Sci.* **2017**, *392*, 777.

[49] S.-Z. Kure-Chu, H. Osaka, H. Yashiro, K. Segawa, K. Wada, S. Inoue, *J. Electrochem. Soc.* **2014**, *162*, C24.

[50] A. L. M. Reddy, M. M. Shaijumon, S. R. Gowda, P. M. Ajayan, *J. Phys. Chem. C* **2010**, *114*, 658.

[51] J. Yue, X. Gu, L. Chen, N. Wang, X. Jiang, H. Xu, J. Yang, Y. Qian, *J. Mater. Chem. A* **2014**, *2*, 17421.